GIScience & Remote Sensing

ISSN: 1548-1603 (Print) 1943-7226 (Online) Journal homepage: www.tandfonline.com/journals/tgrs20

Reconstructing remote sensing reflectance from MODIS-Aqua for enhanced ocean color applications

Tianhao Wang , Wenfang Lu , Zhongping Lee , Xiaolong Yu , Shaoling Shang & Gong Lin

To cite this article: Tianhao Wang , Wenfang Lu , Zhongping Lee , Xiaolong Yu , Shaoling Shang & Gong Lin (2026) Reconstructing remote sensing reflectance from MODIS-Aqua for enhanced ocean color applications, GIScience & Remote Sensing, 63:1, 2681367, DOI: 10.1080/15481603.2026.2681367

To link to this article: https://doi.org/10.1080/15481603.2026.2681367

GISCIENCE & REMOTE SENSING
2026, VOL. 63, NO. 1, 2681367
https://doi.org/10.1080/15481603.2026.2681367

Taylor & Francis by informa

RESEARCH ARTICLE

OPEN ACCESS Check for updates

Reconstructing remote sensing reflectance from MODIS-Aqua for enhanced ocean color applications

Tianhao Wang[a,1], Wenfang Lu[b,1], Zhongping Lee[a], Xiaolong Yu[a], Shaoling Shang[a] and Gong Lin[a]

[a]State Key Laboratory of Marine Environmental Science, College of Ocean and Earth Sciences, Xiamen University, Xiamen, People's Republic of China; [b]School of Marine Sciences, Sun Yat-Sen University, Zhuhai, People's Republic of China

ABSTRACT

Satellite-derived ocean color products are frequently affected by substantial data gaps due to cloud contamination, sun glint, and sensor-related limitations, posing a major challenge for long-term environmental monitoring. To address this, most existing gap-filling efforts have focused on reconstructing inverted variables including chlorophyll-a concentration (CHL) and sea surface temperature. However, this practice is limited by the inflexibility of reconstructing each variable separately. Since CHL and other bio-optical variables are derived from the remote sensing reflectance (R_{rs}) spectrum, reconstructing R_{rs} offers a more general solution. In this study, we propose a spectrally-consistent reconstruction of R_{rs} using the Discrete Cosine Transform with Penalized Least Squares (DCT-PLS) method, applied to MODIS-Aqua daily data over the South China Sea (SCS) for the period of 2010–2020. The reconstructed R_{rs} dataset shows high agreement with in-situ measurements ($R^2 > 0.70$ for most bands) and expands the number of valid satellite–in-situ match-ups by more than four times, especially in persistently cloudy offshore areas. Compared with direct CHL reconstruction (RMSD = 0.63, MAPD = 49.1%), CHL retrieved from reconstructed Rrs shows improved accuracy (RMSD = 0.50, MAPD = 36.4%) based on validation with more than 400 in-situ samples. The reconstructed R_{rs} also enhances long-term trend detectability and signal-to-noise ratios in data-sparse regions. Furthermore, derived bio-optical parameters (e.g. phytoplankton absorption, detrital and gelbstoff absorption, and diffuse attenuation coefficients) exhibit consistent trends, reinforcing the reliability of the reconstructed R_{rs}. Our results demonstrate that reconstructing gap-free R_{rs} datasets not only address data loss but also support the generation of consistent downstream products, enabling reliable long-term monitoring in data-sparse marine environments.

ARTICLE HISTORY
Received 30 December 2025
Accepted 25 May 2026

KEYWORDS
Remote sensing reflectance; sea surface chlorophyll; gap-free datasets; DCT-PLS; South China Sea

1. Introduction

Passive remote sensing via satellites is an indispensable means to observe the Earth's surface repetitively. However, due to the orbit or clouds or failure in data processing, it is common to see data gaps, many times it is very wide, in products distributed by the various satellite missions (Groom et al. 2019; Hu et al. 2019a; Kay, Hedley, and Lavender 2009; Liu and Wang 2022; Stock et al. 2020). This is particularly true for the bio-optical products obtained through satellite ocean colour measurements, which greatly limit the value and application of these satellite products. Missing data not only obscures short-term events like Madden–Julian Oscillation (Wang et al. 2021), but also hampers analyses of seasonal variability and long-term trends (Hong et al. 2023; Wang et al. 2023).

To overcome these limitations, various reconstruction approaches have been developed to recover the missing pixels, but generally focusing on chlorophyll-a concentration (CHL) or sea surface temperature (SST) (Liu and Wang 2019, 2022; Modi, Roxy, and Ghosh 2022; Sirjacobs et al. 2011; Stock et al. 2020). These include spatial interpolation methods, such as Kriging (Oliver and Webster 1990) and optimal interpolation (Kawai and Kawamura, 2006; Reynolds and Smith 1994). There are also empirical orthogonal function (EOF)-based reconstructions (Alvera-Azcárate et al. 2005; Beckers and Rixen 2003), and more recently, deep-learning-based methods (Hong et al. 2023; Martinez et al. 2020; Wang, Zhou, and Li 2025).

CONTACT Zhongping Lee ZhongPing.Lee@umb.edu
[1] Tianhao Wang and Wenfang Lu contributed equally and share first authorship.
Supplemental data for this article can be accessed online at https://doi.org/10.1080/15481603.2026.2681367.

However, CHL represents only one component of the broader suite of bio-optical products retrieved from satellite ocean colour observations, alongside other key variables such as inherent optical properties and suspended particulate matter concentrations. Therefore, it is desirable to fill the spatial gaps of these products also. Since all these bio-optical products are derived from the spectrum of remote sensing reflectance (R_{rs}), as suggested by Marchese et al. (2024) and Lang et al. (2025), a more logical or straightforward route might be to fill the gaps of R_{rs} (Lang et al. 2025; Marchese et al. 2024), then it can lead to many other gap-free products desired by the various users. However, these studies primarily focus on methodological performance or the visual continuity of reconstructed fields, and provide limited analysis of their long-term stability, spectral consistency, and bio-optical validity. From the perspective of R_{rs} reconstruction, important questions remain regarding how reconstructed R_{rs} can support downstream ocean-colour applications. In this study, we aim to exploit the advantages of reconstructing R_{rs} itself and its implications for subsequent bio-optical retrievals and long-term trend analyses.

To investigate these questions, using measurements in the South China Sea (SCS) as an example, we employed a frequency-domain reconstruction approach (Discrete Cosine Transform with Penalised Least Squares, DCT-PLS) to obtain a gap-free R_{rs} dataset. Subsequently, multiple bio-optical parameters are derived from the reconstructed R_{rs}. This is also due to that the daily data loss can exceed 80–90% for SCS (Han et al. 2020; Liu and Wang 2019; Wang et al. 2021), a region with great value to testing and evaluating the limitations of gap-filling methods. It is found that the reconstructed R_{rs} not only matches well with in-situ observations and ensures spectral consistency of R_{rs} spectra, but also enables the derivation of various bio-optical properties that are useful for downstream applications.

2. Data and methods

2.1. Data source

2.1.1. Satellite observations

In this study, we utilised Level-3 (L3) products from the Moderate Resolution Imaging Spectroradiometer onboard the Aqua satellite (MODIS-Aqua), provided by the NASA OceanColor website (https://oceandata.sci.gsfc.nasa.gov/). The study area covers the entire SCS, spanning from 100°E to 125°E and from 0°N to 25°N.

We selected the decade from 2010 to 2020 as an example, during which MODIS-Aqua data quality remained stable and the NASA L3 product pipeline was well-established. This avoids post-2020 orbital drift effects (Feng et al. 2024) and ensures consistency in product processing. We acquired daily R_{rs} at six wavelengths, including bands centred at 412, 443, 488, 531, 547, and 667 nm. These bands are commonly used in ocean colour algorithms to retrieve bio-optical variables. In addition to R_{rs}, the standard CHL product was also downloaded from NASA for the same period. Daily MODIS L3 products at 4 km resolution were used in this study.

The MODIS-Aqua daily R_{rs} dataset over the SCS from 2010 to 2020 exhibits a high overall missing rate of approximately 88%, as shown in Figure 1. The missing rate is quantified as the proportion of invalid pixels relative to the total pixel count within the study domain. This level of data loss is consistent with expectations for single-sensor ocean colour products, especially in tropical regions affected by persistent cloud cover, sun-glint, and so on (Mikelsons and Wang 2019; Ruddick et al. 2014; Wang and Bailey 2001; Wilson and Jetz 2016). For comparison, the blended multi-sensor products (e.g. the Ocean Colour Climate Change Initiative (OC-CCI)) typically report a slightly lower missing rate of around 83.3% through the fusion of multi-sensor observations (Wang et al. 2021). However, blended products may exhibit artificial jumps or inconsistencies due to inter-sensor differences (Hu et al. 2012a; van Oostende et al. 2022), which is why we opted to use single-sensor MODIS data in this study.

2.1.2. In-situ measurements

We utilised an in-situ dataset collected by Xiamen University during 26 cruises conducted across the SCS between 2010 and 2020. A total of 714 surface sampling stations were collected across multiple regions and seasons during these cruises (see Figure 1), forming an independent dataset for ocean colour product evaluation. In-situ R_{rs} measurements were collected following either the above-water approach (Mueller et al. 2000; Zibordi et al. 2012) or the on-water approach (Lee et al. 2019), covering a spectral window of

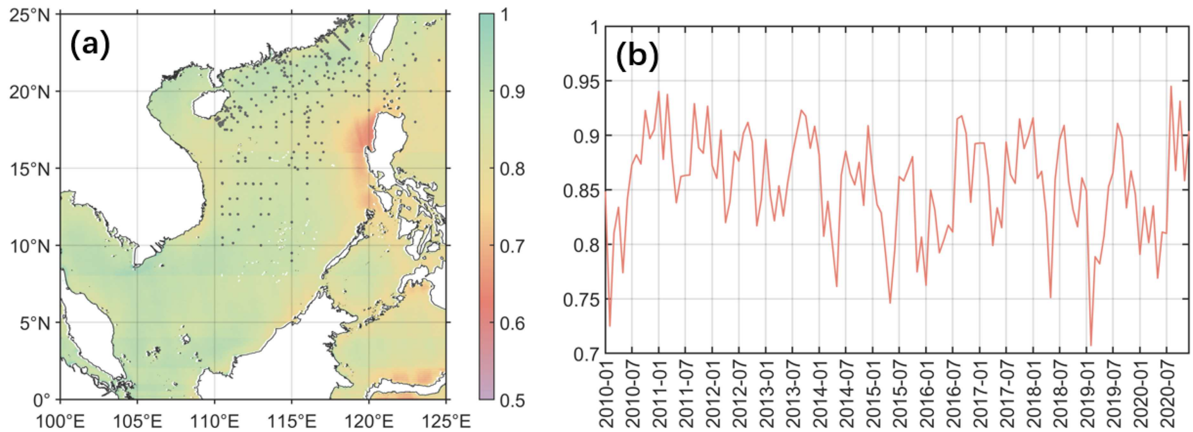

Figure 1. Spatial and temporal missing rate of MODIS R_{rs} products in the SCS over 2010–2020. (a) The spatial distribution of the mean missing rate. Black dots indicate the locations of in-situ sampling stations from 26 cruises. (b) Time series of the missing rate in each month.

approximately 350–900 nm at a resolution of 3–5 nm. CHL were primarily measured following the chlorophyll fluorescence methods (Holm-Hansen et al. 1965; Welschmeyer 1994), with measurements acquired from the upper 5 metres of the water column. Phytoplankton absorption (a_{ph}) was measured using the filter-pad transmittance–reflectance (T–R) method with GF/F filters and a spectrophotometer equipped with an integrating sphere, following IOCCG (2018) recommendations. Absorption by detritus and coloured dissolved organic matter (a_{dg}) was derived from 0.2 µm filtrates measured in a 10 cm cuvette, and converted from optical density to absorption coefficients. The total absorption coefficient (a) was then obtained as the sum of a_{ph}, a_{dg} and pure seawater absorption (Lee et al. 2015).

Considering the increased uncertainties of atmospheric correction in optically complex nearshore waters, as well as the 4 km spatial resolution of the MODIS L3 dataset, in-situ measurements from waters where sea bottom was shallower than 20 m were excluded from the analysis.

To perform satellite-to-in-situ matchups, each in-situ station was spatially and temporally collocated with the MODIS-Aqua L3 mapped daily product. The spatial homogeneity within the 3 × 3 pixel (12 km × 12 km) window was evaluated using the coefficient of variation (CV), defined as the ratio between the standard deviation and the mean value of R_{rs}. Pixels with CV larger than 0.15 were considered heterogeneous and excluded. Using NASA's standard MODIS-Aqua product before reconstruction, we successfully matched 79 MODIS-Aqua pixels to the in-situ observations. With the reconstructed dataset, the number of matched points increased to 371.

2.1.3. Other datasets

To support the interpretation of long-term optical and biological trends in the SCS, two key physical oceanographic variables—sea surface height (SSH) and SST—were incorporated into this study. The SSH dataset was downloaded from CMEMS (the Copernicus Marine Environment Monitoring Service), specifically from the daily Level-4 gridded product, which merges multi-mission satellite altimetry observations. This product provides daily SSH fields with a spatial resolution of 0.125° (approximately 12.5 km), covering the global ocean.

The SST dataset was provided by the NOAA Optimum Interpolation Sea Surface Temperature (OISST) product (version 2.1), a widely used dataset for long-term sea surface temperature analysis. The OISST dataset offers daily fields at a 0.25° resolution, combining satellite infra-red measurements, in-situ data (e.g. buoys, ships), and model outputs through optimum interpolation techniques.

2.2. Methods

2.2.1. Reconstruction method: DCT-PLS

To address the extensive missing data in the daily R_{rs} product and aim to best preserve the spectral signature of an R_{rs} spectrum, we adopted the Discrete Cosine Transform with Penalised Least Squares (DCT-

PLS) method for data reconstruction. This method, originally proposed by Garcia (2010), has been successfully applied to geophysical datasets for its efficiency and robustness in handling spatiotemporal gaps (Guo et al. 2022; Liu et al. 2020; Wang et al. 2012). In studies using CHL datasets in the northern SCS, deep-learning-based approaches such as DINCAE (Data-Interpolating Convolutional Auto-Encoder) have been reported to outperform DINEOF by about 15% (Han et al. 2020), while DCT-PLS achieves improvements of approximately 25% relative to DINEOF (Wang et al. 2021), indicating the strong potential of these methods for ocean colour data reconstruction.

The DCT-PLS approach reconstructs missing data by minimising a cost function that combines two terms: a data fidelity term and a smoothness penalty term. Specifically, let y denote the input 3-D matrix of R_{rs} values. The estimated data matrix $\hat{y}$ is obtained by this formulation:

$$\hat{y} = IDCT\left(\Gamma \circ DCT\left(W \circ (y - \hat{y}) + \hat{y}\right)\right) \tag{1}$$

where $\hat{y}$ and y represent the predicted and original field. DCT and IDCT are discrete cosine transform and its inverse transform. The DCT-PLS method avoids expensive iterative covariance computations by utilising the DCT and IDCT to solve the optimisation problem efficiently in the frequency domain. The reconstruction was performed on the full three-dimensional data cube (longitude, latitude, and time), allowing the DCT-PLS regularisation to exploit both spatial and temporal correlations in the physical field. Further methodological details can be found in Garcia (2010) and Wang et al. (2021). In this study, the DCT-PLS method was applied independently to each variable to reconstruct the six R_{rs} bands (412–667 nm) and CHL.

2.2.2. Accuracy assessment

We evaluated the reconstruction accuracy using several statistical indicators, namely the coefficient of determination (R^2), root mean square difference (RMSD), and mean absolute percentage difference (MAPD):

$$RMSD = \frac{1}{N}\sum_{i=1}^{N}(Y_i - X_i)^2 \tag{2}$$

$$MAPD = \frac{1}{N}\sum_{i=1}^{N}\left|\frac{Y_i - X_i}{X_i}\right| \times 100\% \tag{3}$$

where X_i, Y_i represent the paired physical quantities plotted on the x-axis and y-axis, respectively.

In addition, to evaluate the overall spectral similarity before and after reconstruction, we introduced the Mean Spectral Difference (MSD), defined as follows:

$$MSD = \frac{\left\{\sum_1^n \left[R_{rs}^{rec}(\lambda_i) - R_{rs}^{ori}(\lambda_i)\right]^2\right\}^{0.5}}{\sum_1^n R_{rs}^{ori}(\lambda_i)} \tag{4}$$

where R_{rs}^{ori} and R_{rs}^{rec} represent the R_{rs} from the standard MODIS products and the reconstruction. λ_i represents the wavelength of band i, and n is the number of spectral bands ($n = 6$).

3. Results

3.1. DCT-PLS reconstruction on MODIS R_{rs} products

The DCT-PLS reconstruction performance was quantitatively assessed using a cross-validation dataset comprising 5% of valid MODIS-Aqua daily R_{rs} pixels, randomly withheld from the fitting process. As shown in Figure 2, the reconstructed R_{rs} values were compared with the corresponding original MODIS observations across the six ocean colour wavelengths: 412, 443, 488, 531, 547, and 667 nm, which shows strong consistency with the MODIS data for all bands. Specifically, the R^2 exceeds 0.96 across all bands, with low RMSD (0.0002–0.0005 sr^{-1}) and MAPD mostly below 5%. These results demonstrate the effectiveness of DCT-PLS in resolving the spatiotemporal variability of R_{rs}, even in the presence of extensive missing data. The reconstruction at 667 nm appears to have a lower performance than that at other wavelengths, with a MAPD of 18.1% despite a comparable R^2 of 0.96. Compared to other wavelengths, this relatively higher

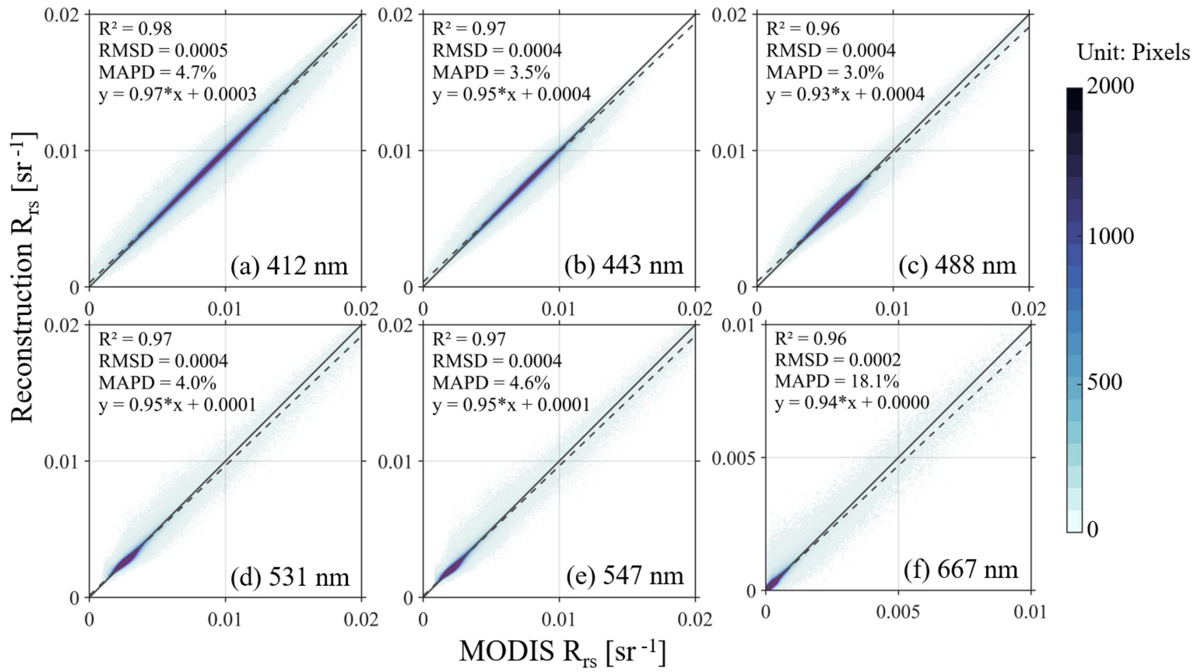

Figure 2. Cross-validation comparison between reconstructed and standard MODIS R_{rs} values across six wavelengths ($N = 6,896,628$). The 1:1 line (solid) and the least-squares regression line (dashed) are shown in each panel.

MAPD is largely attributed to the very low magnitude (close to 0) of R_{rs} at 667 nm (see Figure 2f). As a result, small absolute reconstruction errors are proportionally amplified when expressed in relative terms, thus elevating the percentage-based statistical metrics.

Moreover, the spatial distribution of the MAPD between reconstruction and MODIS R_{rs} for each band is shown in Figure 3. The spatial differences are low and relatively uniform across the SCS, with MAPD values generally below 6% for most regions and wavelengths. Within the SCS basin (depth > 200m), MAPD values are generally low, typically ranging between 2% and 4%. Higher differences are primarily concentrated along coastal zones, island margins, and optically complex regions. These areas are more susceptible to atmospheric correction uncertainty and high spatial variability (Li et al. 2025, Mélin, Zibordi, and Berthon 2007; Song et al. 2023), which would challenge both the original satellite retrieval and the reconstruction process. Among all bands, the 667 nm band shows the most elevated MAPD values, with some localised regions exceeding 10% or more. This is consistent with the findings from the scatterplot analysis (in Figure 2) and is attributed to the intrinsically near-zero value of R_{rs} at this band.

Although the accuracy of reconstructed R_{rs} at individual wavelengths has been shown to be very high, most ocean colour algorithms, particularly those based on spectral ratios or full-spectrum inversion (Garver and Siegel 1997; IOCCG 2006; Lee et al. 1999; Werdell et al. 2013), depend on an R_{rs} spectrum. To evaluate the preservation of spectral shape, the MSD is analysed. As shown in Figure 4, MSD values are generally low throughout the SCS, with most open-ocean areas exhibiting differences below 5%. Figure 4b further illustrates that over 95% of pixels have MSD values below 5%. Such a difference may introduce ~5–15% uncertainty in absorption and ~10–25% in backscattering if applying the Quasi-Analytical Algorithm (QAA_v6, available at https://www.ioccg.org/groups/Software_OCA/QAA_v6_2014209.pdf) (Lee, Carder, and Arnone 2002). These results suggest that DCT-PLS not only achieves good performance in individual-band reconstruction but also preserves spectral coherence, which is essential for reliable downstream bio-optical modelling.

3.2. Evaluation at different missing rates

To quantitatively evaluate the robustness of the DCT-PLS method under varying data availability, artificial gaps were introduced into complete daily R_{rs} datasets to simulate different missing data rates ranging from

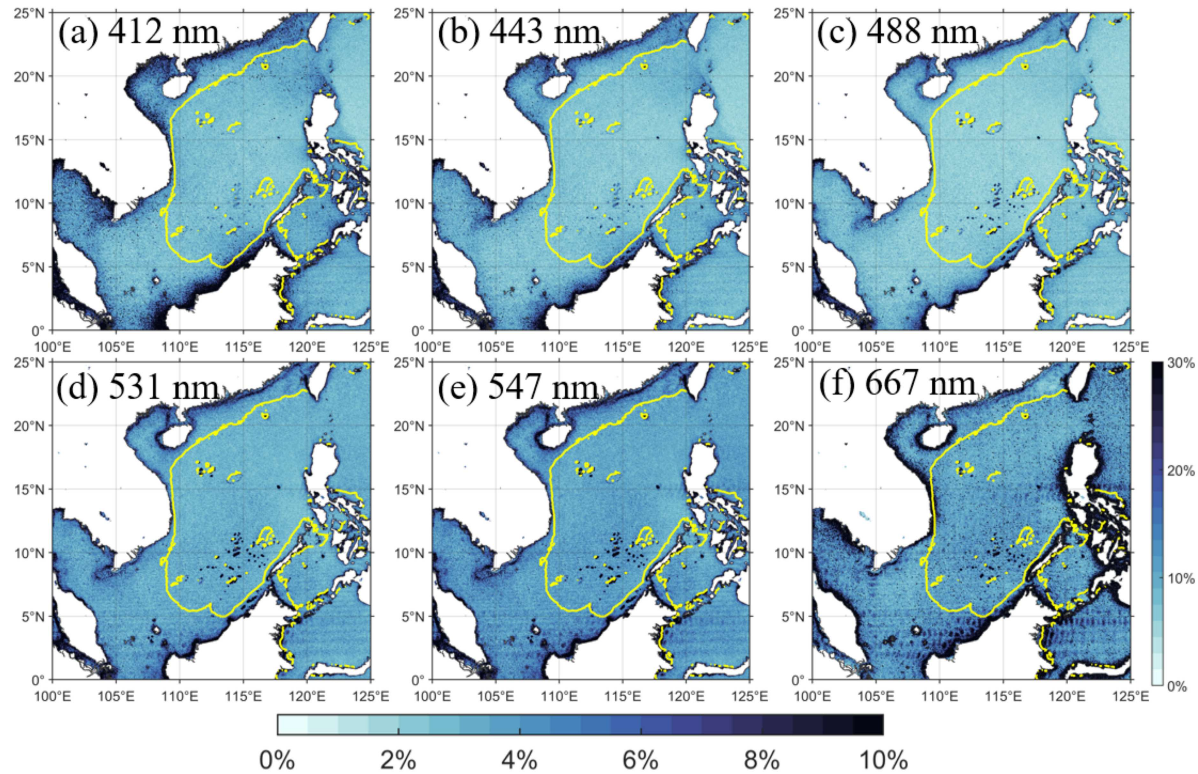

Figure 3. Spatial distribution of MAPD between reconstructed and original MODIS-Aqua R_{rs} values. The yellow line represents the 200-metre isobath, representing the boundary of the basin.

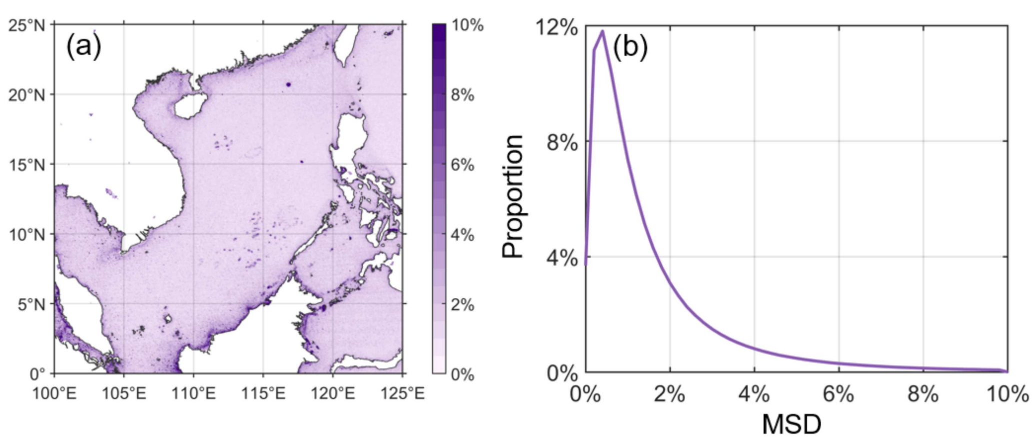

Figure 4. Spatial distribution (a) and statistical profile (b) of the mean spectral difference (MSD) between reconstructed R_{rs} and MODIS R_{rs}.

60% to 98%. Figure 5 presents the MAPD between the reconstructed and original values across three representative bands: 443 nm, 547 nm, and 667 nm. As shown, all three bands exhibit relatively low MAPD values even when missing rates approach 90%. Reconstruction at 443 nm shows the best performance, maintaining MAPD below 4.5% throughout, while the 667 nm band presents the highest MAPD, exceeding 15% in most cases. Overall, the DCT-PLS method demonstrates strong resilience to missing data, particularly for the blue and green bands, which are crucial for downstream biogeochemical applications.

Moreover, Figure 6 provides comparisons of the original MODIS $R_{rs}(443)$ and corresponding reconstructed results for four different days that experienced different missing rates (60%, 70%, 80%, and 90%, respectively). The original MODIS images exhibit progressively larger spatial gaps with increasing missing

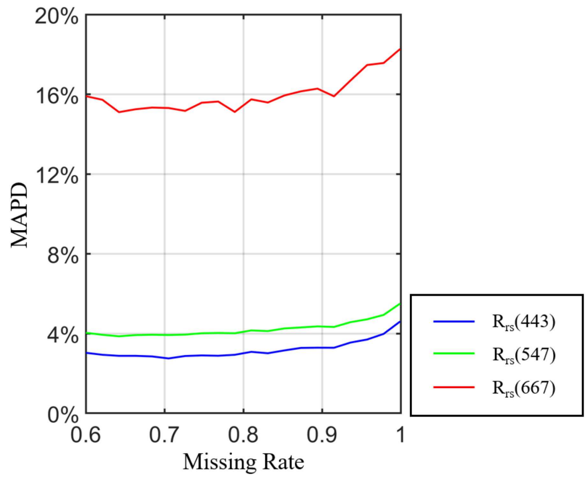

Figure 5. Sensitivity of reconstruction accuracy to missing data rate. Variation in Mean Absolute Percentage Difference (MAPD) of reconstructed R_{rs} at 443 nm, 547 nm, and 667 nm. Artificial missing rates from 0.6 to 0.98 (with a step of 0.01) were used in the sensitivity experiment. For each interval, the reconstruction accuracy was calculated as the average MAPD of all days whose natural missing rates fell within that range.

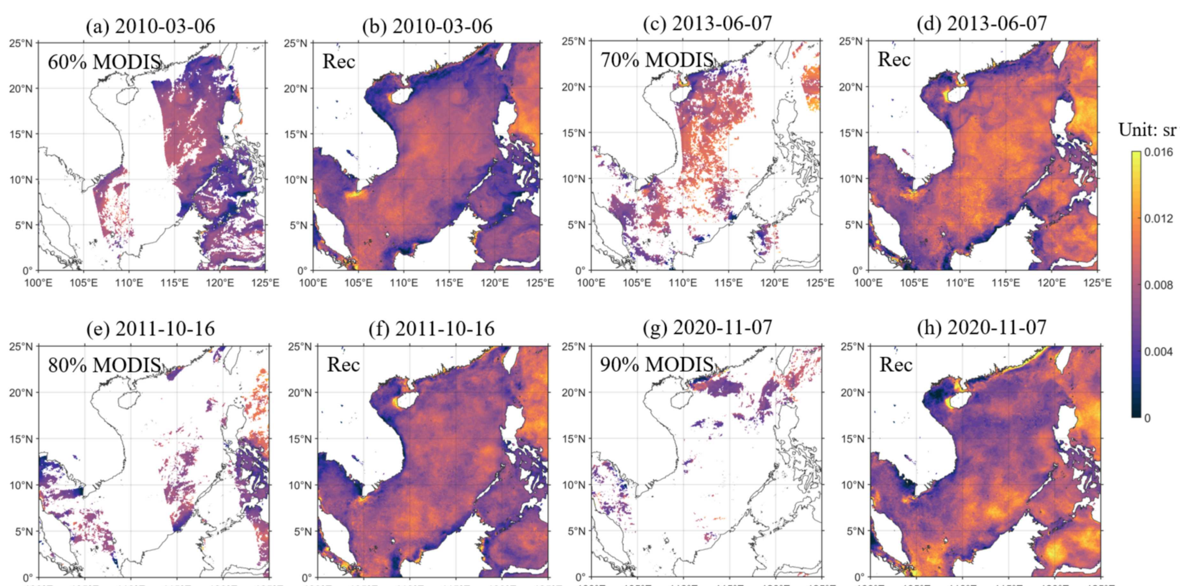

Figure 6. Comparison of MODIS-derived and reconstructed $R_{rs}(443)$ under different missing data rates. Each pair of panels compares the original MODIS L3 $R_{rs}(443)$ data (left) with the corresponding reconstructed result (right) on four representative dates: (a,b) 2010-03-06 (60% missing), (c,d) 2013-06-07 (70%), (e,f) 2011-10-16 (80%), and (g,h) 2020-11-07 (90%).

rates, leaving substantial areas of the SCS unresolved. In contrast, the reconstructed fields present spatially coherent and continuous R_{rs} patterns that retain fine-scale spatial structures across all missing scenarios. Importantly, the reliability of these reconstructed results is further supported by quantitative assessments in Figures 2 to 4, which demonstrate strong consistency between the reconstructed and observed R_{rs}. In addition, the validity of the reconstructed R_{rs} is further evaluated against in-situ observations, which are presented in the subsequent analysis.

Notably, even under extreme data loss conditions (e.g. 90% missing rate, Figure 6g), the reconstruction preserves key spatial features such as low-$R_{rs}(443)$ (<0.002 sr^{-1}) regions along the northern shelf of the SCS and high-$R_{rs}(443)$ (>0.012 sr^{-1}) zones in the deep basin. Similarly, mesoscale gradients observed during spring (March 6, 2010) and summer (June 7, 2013), such as suppressed nearshore R_{rs} and offshore fronts, are well retained after reconstruction. These results demonstrate that the method can effectively recover seasonally and regionally relevant structures by exploiting spatial continuity, even when up to 90% of the original data are missing.

These results underscore the effectiveness of DCT-PLS for reconstructing high-resolution R_{rs} datasets under severe observational constraints. The method offers both low error statistics and visually realistic fields, laying a strong foundation for the derivation of other bio-optical products.

3.3. Evaluation with in-situ R_{rs} measurements

To further examine the reliability of reconstructed R_{rs}, we compiled 371 satellite-to-in-situ matchups across the SCS. For standard MODIS data, only 79 in-situ stations could be matched, largely limited by frequent data gaps associated with cloud contamination and other atmospheric interferences. In contrast, the reconstructed dataset supported complete matchups at all stations, demonstrating a remarkable enhancement in spatial data availability and validation capability.

As shown in Figure 7, the standard MODIS R_{rs} demonstrates high accuracy at most wavelengths, particularly in the green bands (e.g. 547 nm, MAPD = 14.4%), due to its acquisition under clear-sky, low-glint conditions. The reconstructed R_{rs} maintains similarly strong performance, especially at 488–547 nm, with R^2 values consistently above 0.90. Although the reconstructed dataset shows modest declines in several statistical indicators (e.g. ~2% higher in MAPD), and the shorter wavelengths at 412 and 443 nm exhibit comparatively weaker agreement with in-situ measurements, these deviations fall within the anticipated range.

It is worth noting that, unlike MODIS L3 products, which are restricted to clear-sky or otherwise optimal viewing conditions, the reconstruction method attempts to estimate R_{rs} under all environmental scenarios—including periods of cloud cover and sun glints. Given this broader applicability, the slight performance tradeoff is acceptable and demonstrates the robustness of the DCT-PLS method in maintaining data quality while vastly expanding the observational footprint.

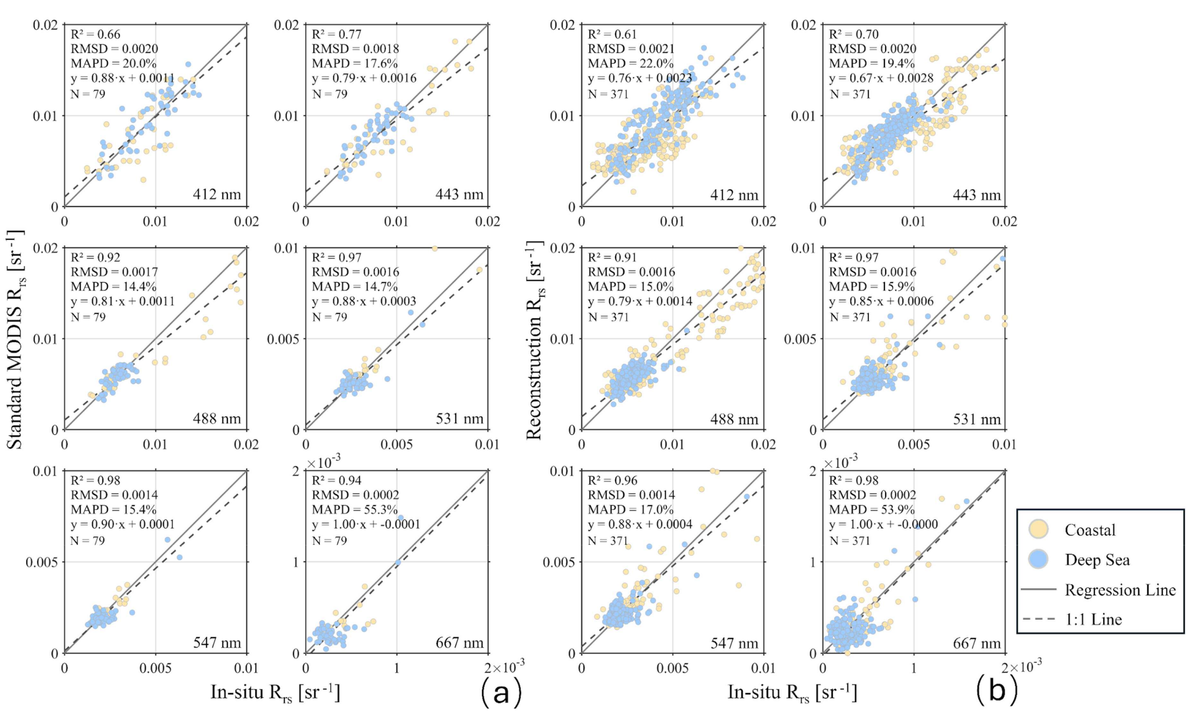

Figure 7. Comparison between in-situ and satellite-derived R_{rs} across six wavelengths. (a) Validation of standard MODIS R_{rs}. (b) Validation of reconstructed R_{rs} using 371 in-situ matchup points. The blue dots represent deep-sea stations (depth > 200 m), while the yellow dots indicate shallow coastal stations (depth < 200 m).

3.4. Application on CHL

To evaluate the applicability of the reconstructed R_{rs} dataset, CHL was selected as a representative bio-optical parameter. We first examined the performance of the standard MODIS CHL product and the reconstructed CHL from the standard CHL also via DCT-PLS, with results shown in Figure 8. In both cases, the satellite estimates show moderate agreement with in-situ data, with R^2 values of 0.66 and 0.69, respectively. While the reconstruction slightly increases data dispersion, it enables a much larger number of valid comparisons. These results suggest that directly reconstructed CHL can preserve the overall statistical characteristics of the original satellite product, while substantially expanding the spatial coverage of available observations, as demonstrated in the literature (Han et al. 2020; Hilborn and Costa 2018; Wang et al. Wang and Gao 2019, 2021).

In addition, we present the comparison between in-situ CHL and CHL estimates produced by the same ocean colour algorithm (OCI) (Hu et al. 2019b; Hu and Lee, 2012b) based on the reconstructed R_{rs} in Figure 8c. It achieves a comparable R^2 (0.68) to direct CHL reconstruction (0.69, in Figure 8b), while significantly reducing RMSD (0.50 vs. 0.63) and MAPD (36.4% vs. 49.1%), especially in low CHL ranges (<0.1 mg m^{-3}). These results highlight the advantage of using reconstructed R_{rs} as the primary input for CHL estimation.

Another important benefit of deriving CHL from reconstructed R_{rs}, rather than reconstructing CHL directly, is the added flexibility it offers in choosing or adjusting bio-optical algorithms. This strategy also facilitates later refinement to regional conditions or algorithm parameters. Although we did not apply any parameter tuning in the present analysis, the use of R_{rs} as the primary variable provides a basis for future advances using region-specific calibrations or machine-learning approaches.

3.5. Application on other products

After validating the reconstructed R_{rs} fields using in-situ CHL measurements and standard CHL retrieval algorithms, we further examined other ocean colour variables derived from the reconstructed R_{rs} datasets. Specifically, we applied the QAA_v6 to retrieve a suite of IOPs, including a and backscattering (b_b) coefficients, a_{dg}(443), and a_{ph}(443). Further, the diffuse attenuation coefficient at 490 nm (K_d(490), m^{-1}) was estimated analytically based on QAA-retrieved a and b_b following Lee et al. (2013), rather than calculated using the band-ratio-based approach from NASA OceanColor.

Figure 9 presents these parameters for two representative dates in 2010 (e.g. first dates ofJanuary, and September). As shown in Figure 9, the standard MODIS L3 products suffer from substantial data loss, especially in winter (Figure 9a), when dense cloud cover and low solar elevation result in large blank areas over the northern SCS. In contrast, the reconstructed datasets yield spatially complete and visually coherent fields across all parameters and dates. This not only improves coverage in previously missing regions but

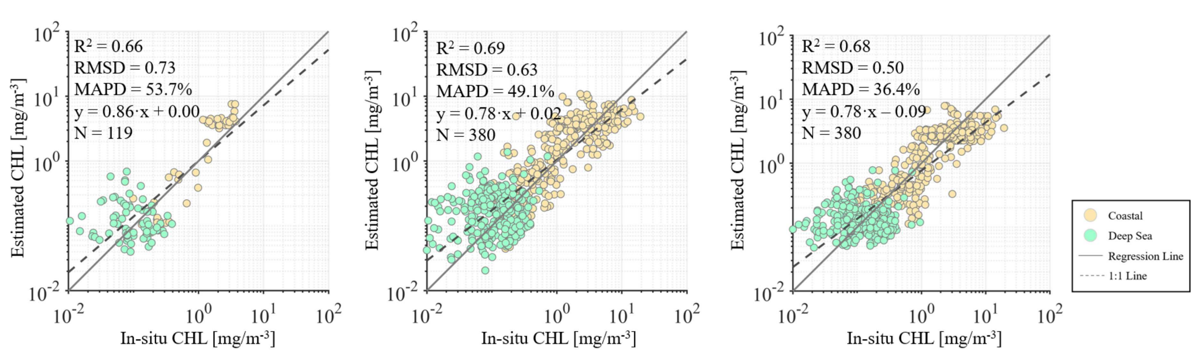

Figure 8. Comparison of satellite-derived CHL with in-situ measurements. (a) Standard MODIS CHL product versus in-situ CHL; (b) Direct reconstruction of CHL (via DCT-PLS) versus in-situ CHL. (c) CHL derived from R_{rs} reconstruction through the OCI algorithm versus in-situ CHL. Green and yellow dots represent shallow (depth < 200 m) and deep (depth > 200 m) water stations, respectively.

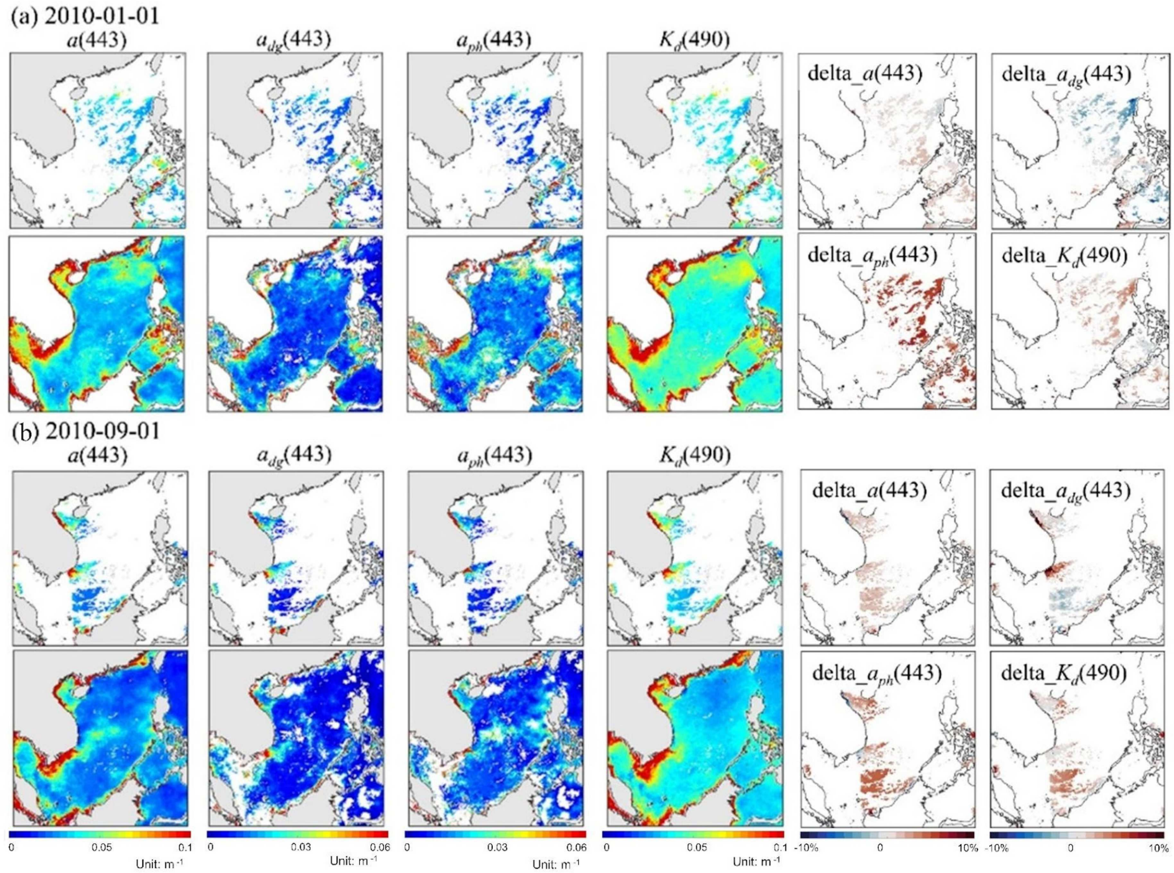

Figure 9. Selected snapshots of absorption and attenuation products derived from standard MODIS (top row of each panel) and reconstructed R_{rs} (bottom row) using the QAA algorithm. Columns show total absorption at 443 nm (a(443)), absorption by coloured detrital and dissolved organic matter (a_{dg}(443)), phytoplankton absorption (a_{ph}(443)), and the diffuse attenuation coefficient (K_d(490)). The images correspond to two representative days in 2010 (January 1st, and September 1st). The corresponding percentage differences (delta_a(443), delta_a_{ph}(443), delta_a_{dg}(443) and delta_K_d(490)) are also shown in the figure, which is computed as IOPs from reconstructed R_{rs} minus IOPs from MODIS L3 R_{rs} divided by IOPs from MODIS L3 R_{rs}. Comparisons for all months in 2010 are shown in Figure R1.

also enhances the spatial consistency of features such as fronts, plumes, and gradients. On a quantitative evaluation, the last two columns in Figure 9 present the percentage differences of the IOP products obtained from standard R_{rs} and reconstructed R_{rs}, showing that the relative difference of the IOPs is generally within 10%, indicating a strong consistency.

We further compared satellite-derived a(443), a_{ph}(443), and a_{dg}(443) with in-situ measurements (see Figure 10). For a(443), IOPs products from reconstructed R_{rs} show a performance comparable to that from the standard MODIS R_{rs} ($R^2 = 0.62$ vs. 0.69, MAPD = 32.3% vs. 31.1% m^{-1}). A similar level of agreement is observed for a_{ph}(443), although with slightly larger uncertainties ($R^2 = 0.51$ vs. 0.56, MAPD = 47.0% vs. 40.4%), which is expected given the increased sensitivity of phytoplankton absorption to spectral variations. For a_{dg}(443), the IOPs from R_{rs} reconstruction show slightly lower MAPD with in-situ observations than the MODIS products (72.5% vs. 83.5%) (Figure 10e,f). All these results suggest that the reconstructed R_{rs} did not negatively affect the overall quality of satellite R_{rs} from MODIS, but the number of matched-up data is 4–5 times larger compared to that of MODIS L3 products.

For coastal regions, the red band (667 nm) plays an important role in QAA, as it is the reference wavelength used to estimate the backscattering coefficients. Therefore, uncertainties in this band may potentially influence the retrieval of IOPs in nearshore environments. However, due to many other factors, such as the non-exact space-time matchups between satellite and in-situ observations, it appears that the performance of QAA using original MODIS R_{rs} and reconstructed R_{rs} is nearly the same.

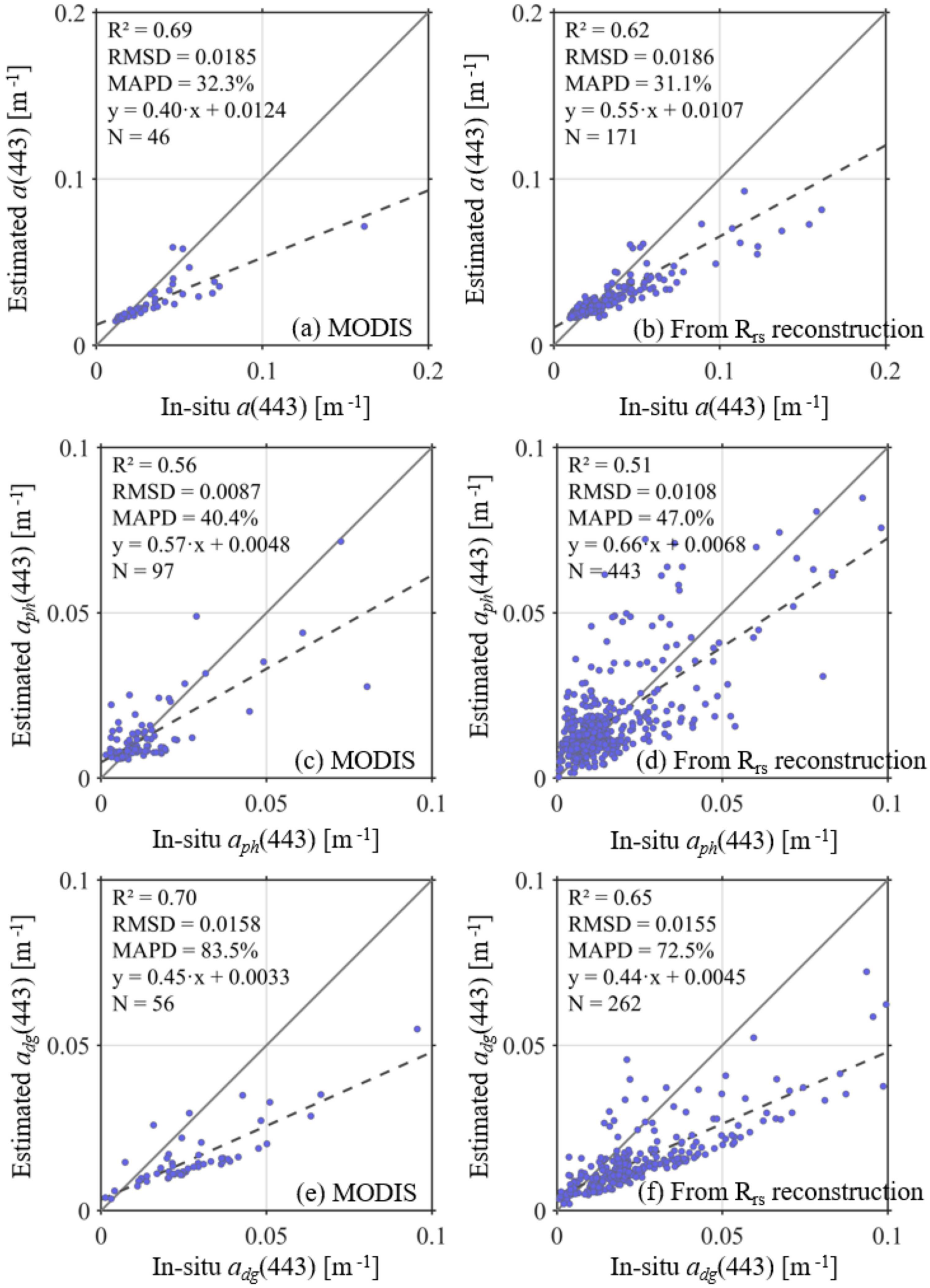

Figure 10. Comparison between in-situ measurements and satellite-derived *a*(443), a_{ph}(443) and a_{dg}(443). Panels (a,b) show *a*(443) from standard MODIS L3 products and derived from reconstructed R_{rs}, respectively. Panels (c,d) are for a_{ph}(443) and Panels (e,f) are for a_{dg}(443). Solid lines indicate the 1:1 relationship and dashed lines represent linear regressions.

With the reconstructed data, pronounced seasonal variability is clearly more evident. For example, high a_{ph}(443) and *a*(443) values are observed along the southern and central coastlines in spring (see Figure 9b,c), reflecting the high productivity of the coastal waters. During summer (see Figure 9d), elevated a_{dg}(443) values appear in regions affected by river runoff, consistent with an enhanced input of land-derived material (Dong, Shang, and Lee 2013; Minu et al. 2020). By autumn (Figure 9e,f), a marked drop in *a* (443) and a_{ph}(443) across offshore waters indicates a shift toward more oligotrophic conditions (Lv et al. 2023; Shen et al. 2008). Seasonal fluctuations in K_d(490) also capture the inverse pattern of water-column transparency, characterised by reduced K_d(490) values during winter and elevated values in summer, indicating clearer waters during the warm season and reduced transparency in winter (Gomes et al. 2018; Shi and Wang 2010).

These results confirm that the reconstructed R_{rs} fields retain not only statistical fidelity but also environmentally meaningful spatial and temporal patterns across multiple optical parameters. This further highlights that the reconstruction framework is not limited to a single product (e.g. CHL), but can be reliably propagated through full-spectrum bio-optical models to support broader applications in environmental monitoring and oceanographic research.

3.6. Trend analysis

3.6.1. R_{rs} and CHL

Recent studies have proved that R_{rs} itself is also a key indicator of climate change (Cael et al. 2023; Dutkiewicz et al. 2019; Huot and Antoine 2016). In Figure 11, we compare the annual trends in $R_{rs}(443)$ and $R_{rs}(547)$ across the SCS from 2010 to 2020, using both the standard MODIS L3 dataset and the reconstructed datasets. For $R_{rs}(443)$, both the standard MODIS and reconstructed datasets exhibit a comparable increasing trend (0.7% and 0.78%) in offshore waters (depth > 200 m), which reflects reduced phytoplankton absorption (Siegel et al. 2002) and enhanced water clarity (Lee et al. 2018).

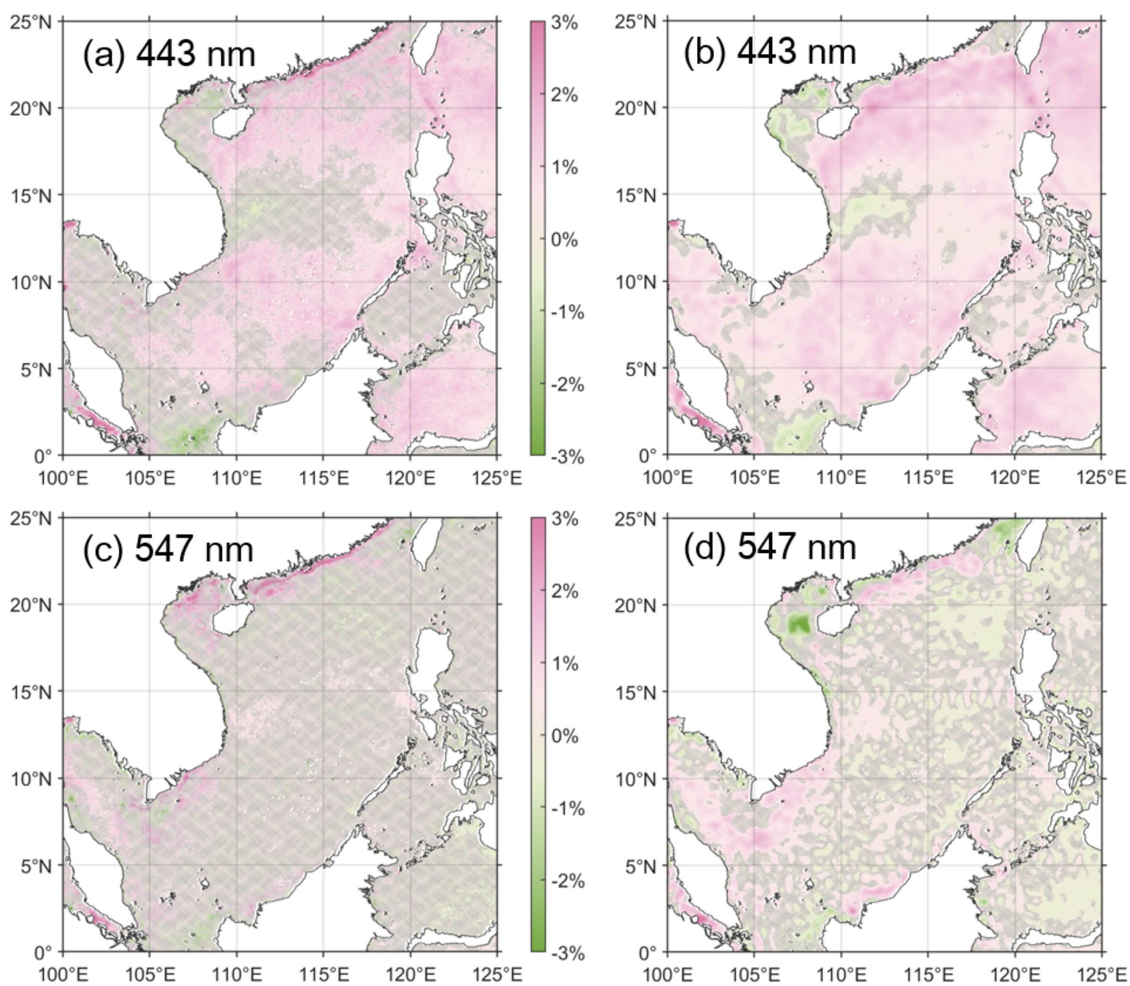

Figure 11. Long-term trends of R_{rs} at 443 nm and 547 nm in the SCS from 2010 to 2020. Panels (a) and (c) show the annual rate of change (% yr^{-1}) for standard MODIS L3 products at 443 nm and 547 nm, respectively, while panels (b) and (d) present the corresponding results based on the reconstructed R_{rs} dataset. Grey-shaded areas indicate regions that did not pass the significance test ($p > 0.05$).

Spatially, while the reconstructed dataset substantially increases data coverage—nearly doubling the area with statistically significant trends compared to standard MODIS products—its greater value lies in enabling robust detection of long-term signals. The reconstructed results reveal coherent and spatially consistent trends even in regions previously obscured by persistent data gaps, suggesting that the reconstructed values are not only spatially complete but also generally reliable for trend analysis.

In contrast, the trend patterns at 547 nm are more spatially heterogeneous and of smaller magnitude. The standard MODIS product shows weak or negligible trends over most of the basin, with localised increases confined to certain coastal regions. However, the reconstructed dataset reveals a more nuanced picture, including not only similar nearshore increases but also new areas of significant decrease, particularly in offshore zones. Quantitatively, the average trend over the entire SCS is 0.10% yr^{-1} for the standard MODIS product and −0.03% yr^{-1} for the reconstruction; for the basin, the difference is 0.06% vs. −0.005% yr^{-1}. All trends discussed here pass the 95% confidence threshold ($p < 0.05$). These differences indicate that the reconstructed dataset alters some of the original trend patterns due to the filling of missing satellite observations, and more importantly, enhances the detection of previously obscured or weak signals.

As mentioned earlier, the rise of $R_{rs}(443)$ in the SCS basin indicates that phytoplankton absorption is weakened (Figure 11a,b), which is consistent with the observed decreasing trend of $a_{ph}(443)$ (not shown here). This optical feature corresponds to a basin-wide reduction of CHL in the basin, which also proves the reliability of the reconstructed product (Figure 12a,b), and reflects a distinct regional process embedded within the broader basin-wide oligotrophic trend.

However, the Vietnam Jet region is an exception, where $R_{rs}(443)$ decreases (red box in Figure 11b), and CHL rises (red box in Figure 12b). This increase in CHL may be driven by the monsoon dynamics associated with the Vietnam jet. The southwest monsoon promotes the formation of a nearshore jet and Ekman divergence, resulting in the shallowing of the SSH depression and mixed layer (Figure 12c), which enhances nutrient fluxes into the euphotic zone, leading to increased phytoplankton productivity. On the contrary, SST rose slightly in the whole SCS (Figure 12d), indicating that thermal stratification is not the main control factor around the Vietnam Jet. These regional trends of R_{rs} are closely related to the changes of CHL and other derived parameters, which strengthens the role of R_{rs} as a basic variable for integrating various biogeochemical signals in the upper ocean.

In conclusion, combined with CHL, SSH, and SST, we found that the trend of the reconstructed R_{rs} dataset can offer improved insight into the coupling between physical processes and biogeochemical variability in the region. These trends do not reflect the characteristics of a single variable, but the response of the ecosystem to monsoon-driven circulation, sea level rise and fall, and other changes, indicating the importance of R_{rs} reconstruction for detecting regional long-term trends.

3.6.2. Signal-to-noise ratio of R_{rs} trends

After the trend analysis, we are also concerned about the significance of these trends. Following the multi-band method proposed by Cael et al. (2023), we further evaluated the stability of the detected long-term trend signal by calculating the signal-to-noise ratio (SNR) of the R_{rs} trend, which was computed as the ratio between the norm of the trend vector and the uncertainty projected along the same direction, as derived from its covariance matrix. In this method, the SNR is a combination of the information of multiple spectral bands to quantify the intensity of the long-term trend relative to the background change. Here, we used R_{rs} products at six bands (412, 443, 488, 531, 547, and 667 nm) to provide a comprehensive spectral evaluation of trend detectability. While the trend slope represents the direction and magnitude of change, the SNR characterises the statistical confidence with which such changes can be distinguished from natural fluctuations.

The SNR distribution exhibits distinct spatial patterns between standard MODIS L3 R_{rs} products and the reconstruction. In the standard MODIS product (Figure 13a), high SNR values are mostly confined to limited coastal regions, while large portions of the basin—especially in the central and northeastern South China Sea—show weak or statistically insignificant signals. In contrast, the reconstructed dataset (Figure 13b) presents a much more coherent and extensive SNR field, with notably enhanced values across the open-ocean basin and along dynamic circulation features. In particular, a clear high-SNR band appears east of Hainan Island, coinciding with the region influenced by the Hainan coastal current and associated eddy activity. Elevated SNRs are also observed along the western boundary and around the Vietnam Jet pathway,

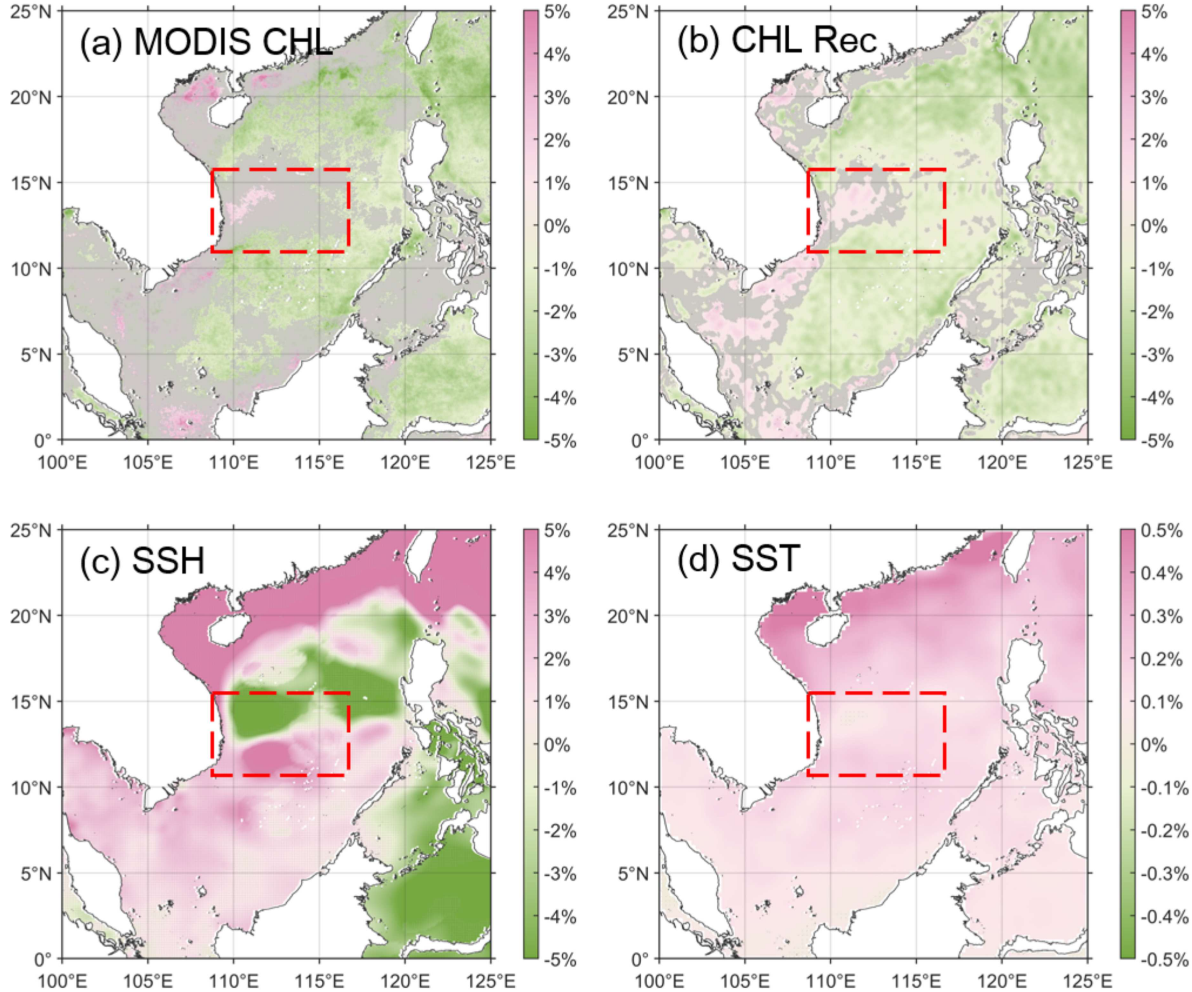

Figure 12. Same as Figure 11, but for (a) standard MODIS CHL product, (b) CHL derived from R_{rs} reconstruction, (c) sea surface height, (d) sea surface temperature. The red boxes represent the Vietnam Jet region.

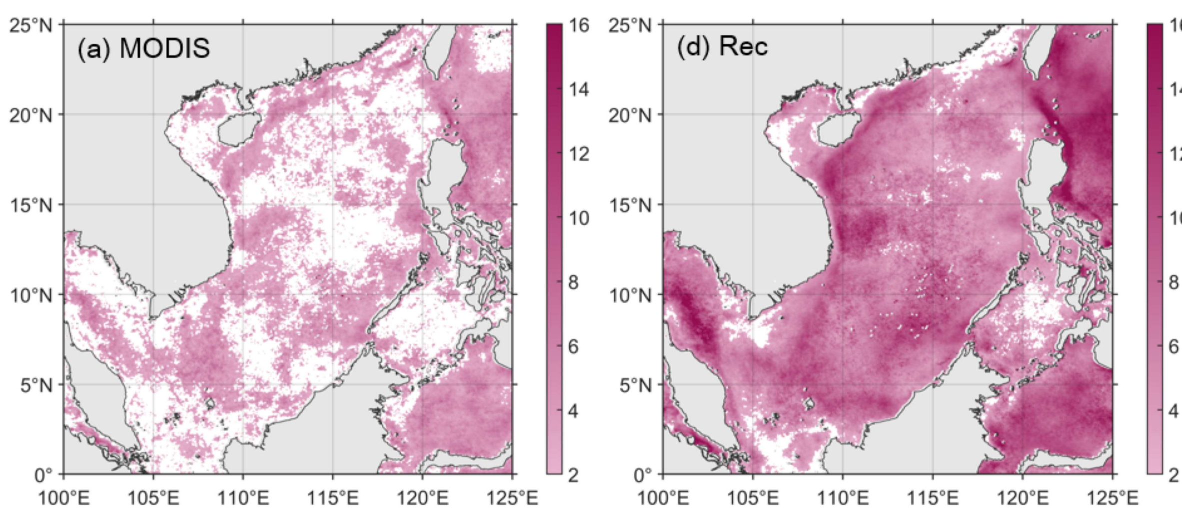

Figure 13. Trend of the signal-to-noise of R_{rs}. The pixels with SNR < 2 are denoted as white dots. The SNR is calculated following Cael et al. (2023).

suggesting that reconstruction effectively strengthens trend detection in regions strongly modulated by mesoscale and seasonal processes.

Moreover, these findings align with the spatial patterns discussed in Figure 12: the standard product often yields fragmented or statistically ambiguous trends, the reconstruction provides smoother and more statistically confident patterns. This enhancement likely reflects a more complete and consistent time series that reduces noise in slope estimation.

Overall, this analysis highlights a key advantage of R_{rs}-level reconstruction—not just in recovering missing data, but in reinforcing the detectability of subtle environmental changes that may otherwise remain undetected in conventional satellite products.

3.6.3. Trend of IOPs

In addition to R_{rs}, we examined long-term trends in three key derived optical parameters—a_{ph}(443), a_{dg}(443), and K_d(490)—which offer insights into underlying biogeochemical processes (Figure 14) (Favareto et al. 2018; Valente et al. 2022; Werdell et al. 2018). As a proxy for phytoplankton pigment absorption, a_{ph}(443) reflects changes in CHL and phytoplankton biomass (Bricaud et al. 1995; Lee, Carder, and Arnone 2002; Sathyendranath and Platt 1998). Both the standard MODIS and the reconstructed R_{rs} showed a downward trend of a_{ph}(443), especially in the northern SCS and coastal regions (Figure 14a,b), suggesting a decadal decrease in primary productivity. The averaged decrease is −0.92% yr^{-1} for the standard MODIS product and −0.83% yr^{-1} for a_{ph}(443) from R_{rs} reconstruction. The trend range of reconstruction results is usually lower than that of standard products, and is close to half in some areas. This difference may reflect the smoothing effect of reconstruction, thus reducing noise and data discontinuity.

Moreover, the original and reconstructed a_{dg}(443) datasets tend to increase in estuaries and coastal waters, which may be related to enhanced land runoff, organic decomposition or nearshore mixing processes (Figure 14c,d), while basin-averaged rates are −0.24% yr^{-1} for the standard MODIS product and −0.19% % yr^{-1} for a_{dg}(443) from R_{rs} reconstruction. Compared with the standard product (Figure 14c), the reconstructed a_{dg}(443) shows more continuous characteristics (Figure 14d), including strong seasonal phenomena, such as the pattern of the Vietnam jet. This indicates that the reconstruction can enhance the trend signal of a_{dg}(443), and further reflect the subtle changes of CDOM and particulate debris concentration, which are also the key indicators of land input, organic matter degradation and other processes (Bonelli et al. 2021; Schwarz and Kowalczuk, 2002; Wei et al. 2019; Yu et al. 2019).

In addition to the absorption-related parameters, the change of K_d(490) (Figure 14e,f) is closely related to the changes of water transparency, phytoplankton, CDOM and suspended particulate matter (Lee and Darecki, 2005b; Son and Wang 2015; Wang, Son, and Harding 2009). Both datasets show broadly decreasing trends in offshore regions and weak increases along select coastal margins (Figure 14e,f). Quantitatively, the trend differs between offshore and coastal regions. In offshore waters (depth > 200 m), the basin-mean trend is −0.23% yr^{-1} for the standard MODIS product and −0.15% yr^{-1} for K_d(490) from R_{rs} reconstruction, whereas in coastal regions (depth < 200 m), the corresponding values are 0.17% yr^{-1} and 0.13% yr^{-1}, respectively. These patterns indicate a general improvement in offshore clarity and localised turbidity enhancements nearshore (Lee and Du, 2005a, Lee and Darecki, 2005b; Yang, Ye, and Tang 2020). It should be noted that the reconstructed K_d(490) shows that these patterns have greater spatial continuity, especially in the areas where previously missing values were dominant (Figure 1a). This enhancement can identify subtle but environmentally significant trends, further proving the benefits of R_{rs} reconstruction for long-term monitoring of the upper-ocean optical variability.

In summary, the IOPs dataset derived from the reconstructed R_{rs} not only preserves the main spatial patterns of long-term trends observed in the original MODIS products but also reveals broader changes among multiple optical parameters. The trends of a_{ph}(443), a_{dg}(443), and K_d(490) obtained from the reconstructed R_{rs} show clearer spatial consistency and enhance sensitivity to subtle changes in phytoplankton biomass, suspended matter, and water transparency. These results indicate that R_{rs} reconstruction can provide a more complete and detailed explanation of long-term ocean colour changes, especially in regions and seasons where standard products are limited by data gaps.

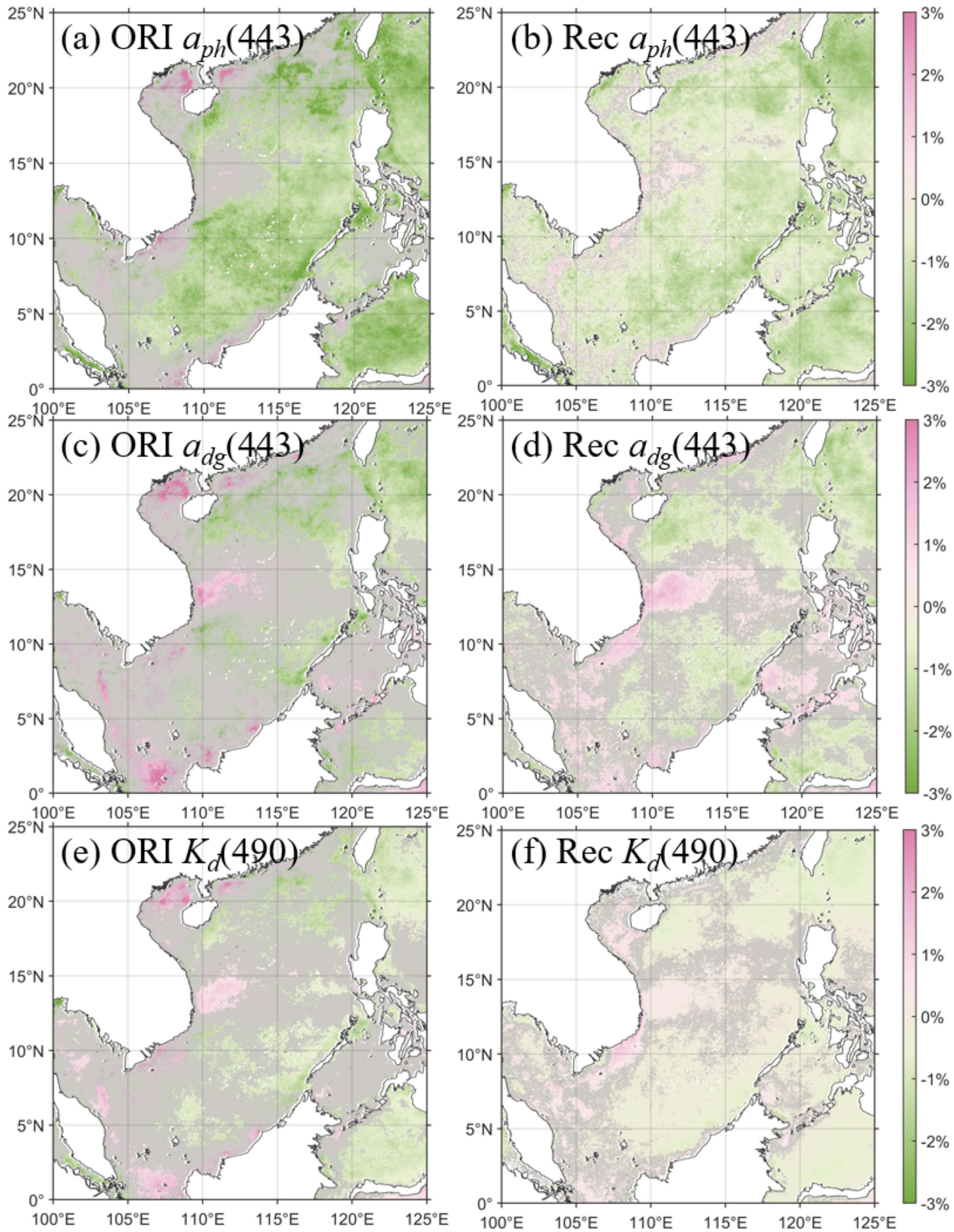

Figure 14. Same as Figure 11, but for $a_{ph}(443)$, $a_{dg}(443)$ and $K_d(490)$.

4. Conclusions

In this study, using measurements in the SCS as an example, we generated gapless R_{rs} products by applying the DCT-PLS method to recover the missing observations. Compared with the standard MODIS L3 product, the reconstructed R_{rs} datasets not only improve spatial coverage and temporal continuity, especially in areas with persistent clouds, but also enhance the overall quality and practicality of ocean colour observations. These improvements are evident in three key dimensions: accuracy, flexibility, and spatio-temporal consistency.

In terms of accuracy, the reconstructed R_{rs} are highly consistent with MODIS and in-situ measurements, and increased the satellite-in-situ matchups fourfold compared to those based on standard MODIS products. This expanded data availability provides a stronger foundation for retrieving key ocean colour parameters and conducting subsequent assessments and applications. The reconstructed R_{rs} dataset enhances flexibility by providing spectrally consistent inputs for a wide range of bio-optical algorithms, supporting the retrieval of CHL as well as IOPs. In addition, the reconstructed R_{rs} dataset not only demonstrates high spatiotemporal consistency in reflecting ocean dynamics, but also preserves internal consistency across derived bio-optical variables, supporting more accurate and coherent environmental assessments.

Furthermore, the reconstruction improves accuracy and consistency CHL and other optical variables derived from reconstructed R_{rs}, enabling more coherent detection of long-term trends. Notably, trend analyses reveal broader regions of statistically significant R_{rs} changes and consistently higher signal-to-noise ratios in offshore and dynamically active areas. These results demonstrate that the reconstruction focusing on R_{rs} can enhance the utility of satellite ocean colour observations.

Nevertheless, some limitations of the current approach should also be acknowledged. Although DCT-PLS demonstrates good reconstruction accuracy and high computational efficiency, it may introduce some degree of smoothing in regions with strong spatial variability. Future work could combine this framework with deep-learning-based approaches to better preserve fine-scale features while maintaining stable gap reconstruction.

Beyond methodological improvements, future work could extend this framework to multi-sensor ocean colour observations to generate longer and spectrally consistent R_{rs} records. Such datasets would be valuable for regional ecosystem monitoring, detection of short-term extreme events, and validation or assimilation of biogeochemical models, particularly in regions where persistent cloud cover limits standard satellite observations.

Author contributions

CRediT: **Tianhao Wang:** Conceptualization, Data curation, Formal analysis, Methodology, Software, Validation, Visualization, Writing – original draft, Writing – review & editing; **Wenfang Lu:** Conceptualization, Writing – original draft, Writing – review & editing; **Zhongping Lee:** Conceptualization, Supervision, Writing – original draft, Writing – review & editing; **Xiaolong Yu:** Writing – review & editing; **Shaoling Shang:** Writing – review & editing; **Gong Lin:** Data curation.

Disclosure statement

The authors declare that they have no known competing financial interests or personal relationships that could have appeared to influence the work reported in this paper.

Funding

This work was supported by the National Key Research and Development Programme of China (2023YFC3107603, 2022YFC3104901, 2022YFC3104903), the National Natural Science Foundation of China (42376173 and 42430107), and the Fundamental Research Funds for the Central Universities (20720240102) and the MEL Internal Program (MELRI2602 and MELRI2605). We also thank Ms. Ying Su for her assistance during the execution of the above projects. A portion of the data and samples was collected during the open research cruises NORC2023-11, NORC2025-02, NORC2024-04, supported by NSFC Shiptime Sharing Project (project numbers: 42249911, 42449902, 42349904).

Data availability statement

The satellite ocean colour data used in this study are publicly available from the NASA OceanColor repository. Specifically, the MODIS-Aqua Level-3 remote sensing reflectance and chlorophyll-a products were obtained from NASA OceanColor (https://oceancolor.gsfc.nasa.gov/), which provides open-access datasets under a CC-BY–compatible license.

The in-situ measurements used in this study, including remote sensing reflectance and chlorophyll-a data collected by the authors' research group, have been deposited in http://doi.org/10.5281/zenodo.18084640 (Wang 2025). These datasets include all values required to reproduce the analyses and figures presented in this article.

References

Alvera-Azcárate, A., A. Barth, M. Rixen, and J.-M. Beckers. 2005. "Reconstruction of Incomplete Oceanographic Data Sets Using Empirical Orthogonal Functions: Application to the Adriatic Sea Surface Temperature." *Ocean Modelling* 9: 325–346. https://doi.org/10.1016/j.ocemod.2004.08.001.

Beckers, J.-M., and M. Rixen. 2003. "EOF Calculations and Data Filling from Incomplete Oceanographic Datasets." *Journal of Atmospheric Oceanic Technology* 20: 1839–1856. https://doi.org/10.1175/1520-0426(2003)020<1839:ECADFF>2.0.CO;2.

Bonelli, A. G., V. Vantrepotte, D. S. F. Jorge, J. Demaria, C. Jamet, D. Dessailly, A. Mangin, O. F. d'Andon, E. Kwiatkowska, and H. Loisel. 2021. "Colored Dissolved Organic Matter Absorption at Global Scale from Ocean Color Radiometry Observation: Spatio-Temporal Variability and Contribution to the Absorption Budget." *Remote Sensing of Environment* 265: 112637. https://doi.org/10.1016/j.rse.2021.112637.

Bricaud, A., M. Babin, A. Morel, and H. Claustre. 1995. "Variability in the Chlorophyll-Specific Absorption Coefficients of Natural Phytoplankton: Analysis and Parameterization." *Journal of Geophysical Research: Oceans* 100: 13321–13332. https://doi.org/10.1029/95JC00463.

Cael, B., K. Bisson, E. Boss, S. Dutkiewicz, and S. Henson. 2023. "Global Climate-Change Trends Detected in Indicators of Ocean Ecology." *Nature* 619: 551–554. https://doi.org/10.1038/s41586-023-06321-z.

Dong, Q., S. Shang, and Z. Lee. 2013. "An Algorithm to Retrieve Absorption Coefficient of Chromophoric Dissolved Organic Matter from Ocean Color." *Remote Sensing of Environment* 128: 259–267. https://doi.org/10.1016/j.rse.2012.10.013.

Dutkiewicz, S., A. E. Hickman, O. Jahn, S. Henson, C. Beaulieu, and E. Monier. 2019. "Ocean Colour Signature of Climate Change." *Nature Communications* 10: 578. https://doi.org/10.1038/s41467-019-08457-x.

Favareto, L. R., N. Rudorff, M. Kampel, R. Frouin, R. Röttgers, D. Doxaran, H. Murakami, and C. Dupouy. 2018. "Bio-Optical Characterization and Ocean Colour Inversion in the Eastern Lagoon of New Caledonia, South Tropical Pacific." *Remote Sensing* 10: 1043. https://doi.org/10.3390/rs10071043.

Feng, S., A. Wehrlé, J. M. Cook, A. M. Anesio, J. E. Box, L. G. Benning, and M. Tranter. 2024. "The Apparent Effect of Orbital Drift on Time Series of MODIS MOD10A1 Albedo on the Greenland Ice Sheet." *Science of Remote Sensing* 9: 100116. https://doi.org/10.1016/j.srs.2023.100116.

Garcia, D. 2010. "Robust Smoothing of Gridded Data in One and Higher Dimensions with Missing Values." *Computational Statistics Data Analysis* 54: 1167–1178. https://doi.org/10.1016/j.csda.2009.09.020.

Garver, S. A., and D. A. Siegel. 1997. "Inherent Optical Property Inversion of Ocean Color Spectra and Its Biogeochemical Interpretation: 1. Time Series from the Sargasso Sea." *Journal of Geophysical Research: Oceans* 102: 18607–18625. https://doi.org/10.1029/96JC03243.

Gomes, A. C. C., N. Bernardo, A. C. do Carmo, T. Rodrigues, and E. Alcântara. 2018. "Diffuse Attenuation Coefficient Retrieval in CDOM Dominated Inland Water with High chlorophyll-a Concentrations." *Remote Sensing* 10: 1063. https://doi.org/10.3390/rs10071063.

Groom, S., S. Sathyendranath, Y. Ban, S. Bernard, R. Brewin, V. Brotas, C. Brockmann, P. Chauhan, J.-k Choi, and A. Chuprin. 2019. "Satellite Ocean Colour: Current Status and Future Perspective." *Frontiers in Marine Science* 6: 485. https://doi.org/10.3389/fmars.2019.00485.

Guo, X., X. Fang, Y. Cao, L. Yang, L. Ren, Y. Chen, and X. Zhang. 2022. "Reconstruction of ESA CCI Soil Moisture Based on DCT-PLS and in Situ Soil Moisture." *Hydrology Research* 53: 1221–1236. https://doi.org/10.2166/nh.2022.058.

Han, Z., Y. He, G. Liu, and W. Perrie. 2020. "Application of Dincae to Reconstruct the Gaps in chlorophyll-a Satellite Observations in the South China Sea and West Philippine Sea." *Remote Sensing* 12: 480. https://doi.org/10.3390/rs12030480.

Hilborn, A., and M. Costa. 2018. "Applications of DINEOF to Satellite-Derived chlorophyll-a from a Productive Coastal Region." *Remote Sensing* 10: 1449. https://doi.org/10.3390/rs10091449.

Holm-Hansen, O., C. J. Lorenzen, R. W. Holmes, and J. D. Strickland. 1965. "Fluorometric Determination of Chlorophyll." *ICES Journal of Marine Science* 30: 3–15. https://doi.org/10.1093/icesjms/30.1.3.

Hong, Z., D. Long, X. Li, Y. Wang, J. Zhang, H. A. Mohamed, and M. M. A. Mohamed. 2023. "A Global Daily Gap-Filled chlorophyll-a Dataset in Open Oceans during 2001–2021 from Multisource Information Using Convolutional Neural Networks." *Earth System Science Data Discussions* 2023: 1–28.

Hu, C., Z. Lee, and B. Franz. 2012b. "Chlorophyll a Algorithms for Oligotrophic Oceans: A Novel Approach Based on Three-Band Reflectance Difference." *Journal of Geophysical Research: Oceans* 117(C1): C01011.

Hu, C., B. B. Barnes, L. Feng, M. Wang, and L. Jiang. 2019a. "On the Interplay between Ocean Color Data Quality and Data Quantity: Impacts of Quality Control Flags." *IEEE Geoscience and Remote Sensing Letters* 17: 745–749. https://doi.org/10.1109/LGRS.2019.2936220.

Hu, C., L. Feng, Z. Lee, C. O. Davis, A. Mannino, C. R. McClain, and B. A. Franz. 2012a. "Dynamic Range and Sensitivity Requirements of Satellite Ocean Color Sensors: Learning from the Past." *Applied Optics* 51: 6045–6062. https://doi.org/10.1364/AO.51.006045.

Hu, C., L. Feng, Z. Lee, B. A. Franz, S. W. Bailey, P. J. Werdell, and C. W. Proctor. 2019b. "Improving Satellite Global Chlorophyll a Data Products through Algorithm Refinement and Data Recovery." *Journal of Geophysical Research: Oceans* 124: 1524–1543. https://doi.org/10.1029/2019JC014941.

Huot, Y., and D. Antoine. 2016. "Remote Sensing Reflectance Anomalies in the Ocean." *Remote Sensing of Environment* 184: 101–111. https://doi.org/10.1016/j.rse.2016.06.002.

Kawai, Y., H. Kawamura, S. Takahashi, K. Hosoda, H. Murakami, M. Kachi, and L. Guan. 2006. "Satellite-Based High-Resolution Global Optimum Interpolation Sea Surface Temperature Data." *Journal of Geophysical Research: Oceans* 111: C06016.

Kay, S., J. D. Hedley, and S. Lavender. 2009. "Sun Glint Correction of High and Low Spatial Resolution Images of Aquatic Scenes: A Review of Methods for Visible and Near-Infrared Wavelengths." *Remote Sensing* 1: 697–730. https://doi.org/10.3390/rs1040697.

Lang, S., Y. Jiang, S. Wang, Y. Jia, and Y. Zhang. 2025. "Reconstructing Gap-Free Daily Remote Sensing Reflectance in the Marginal Seas Using the DINEOF Method." *IEEE Journal of Selected Topics in Applied Earth Observations and Remote Sensing* 18: 11588–11598. https://doi.org/10.1109/JSTARS.2025.3563216.

Lee, Z-P, IOCCG. 2006. Remote Sensing of Inherent Optical Properties: Fundamentals, Tests of Algorithms, and Applications. In *Reports of the International Ocean-Colour Coordinating Group, No. 5*. Dartmouth, Canada: IOCCG.

Lee, Z., K. L. Carder, and R. A. Arnone. 2002. "Deriving Inherent Optical Properties from Water Color: A Multiband Quasi-Analytical Algorithm for Optically Deep Waters." *Applied Optics* 41: 5755–5772. https://doi.org/10.1364/AO.41.005755.

Lee, Z., K. L. Carder, C. D. Mobley, R. G. Steward, and J. S. Patch. 1999. "Hyperspectral Remote Sensing for Shallow Waters: 2. Deriving Bottom Depths and Water Properties By Optimization." *Applied Optics* 38: 3831–3843. https://doi.org/10.1364/AO.38.003831.

Lee, Z., K. Du, R. Arnone, S. Liew, and B. Penta. 2005a. "Penetration of Solar Radiation in the Upper Ocean: A Numerical Model for Oceanic and Coastal Waters." *Journal of Geophysical Research: Oceans* 110: C09019.

Lee, Z. P., M. Darecki, K. L. Carder, C. O. Davis, D. Stramski, and W. J. Rhea. 2005b. "Diffuse Attenuation Coefficient of Downwelling Irradiance: An Evaluation of Remote Sensing Methods." *Journal of Geophysical Research: Oceans* 110: C02017.

Lee, Z., J. Wei, K. Voss, M. Lewis, A. Bricaud, and Y. Huot. 2015. "Hyperspectral Absorption Coefficient of "pure" Seawater in the Range of 350–550 Nm Inverted from Remote Sensing Reflectance." *Applied Optics* 54: 546–558. https://doi.org/10.1364/AO.54.000546.

Lee, Z., C. Hu, S. Shang, K. Du, M. Lewis, R. Arnone, and R. Brewin. 2013. "Penetration of UV-visible Solar Radiation in the Global Oceans: Insights from Ocean Color Remote Sensing." *Journal of Geophysical Research: Oceans* 118: 4241–4255. https://doi.org/10.1002/jgrc.20308.

Lee, Z., S. Shang, K. Du, B. Liu, G. Lin, J. Wei, and X. Li. 2018. "Enhance Field Water-Color Measurements with a Secchi Disk and Its Implication for Fusion of Active and Passive Ocean-Color Remote Sensing." *Applied Optics* 57: 3463–3473. https://doi.org/10.1364/AO.57.003463.

Lee, Z., J. Wei, Z. Shang, R. Garcia, H. Dierssen, J. Ishizaka, and A. Castagna. 2019. On-Water Radiometry Measurements: Skylight-Blocked Approach and Data Processing. Appendix to Protocols for Satellite Ocean Colour Data Validation. In *Situ Optical Radiometry. IOCCG Ocean Optics and Biogeochemistry Protocols for Satellite Ocean Colour Sensor Validation, 3*, 7.

Li X., Lee Z., Wang D., and Shang S. 2025. "Atmospheric correction of coastal waters based on satellite-AERONET-OC matchups via neural networks." *Journal of Remote Sensing 5*: 0886.

Liu, X., and M. Wang. 2019. "Filling the Gaps of Missing Data in the Merged VIIRS SNPP/NOAA-20 Ocean Color Product Using the DINEOF Method." *Remote Sensing* 11: 178. https://doi.org/10.3390/rs11020178.

Liu, X., and M Wang. 2022. "Global Daily Gap-Free Ocean Color Products from Multi-Satellite Measurements." *International Journal of Applied Earth Observation and Geoinformation* 108: 102714. https://doi.org/10.1016/j.jag.2022.102714.

Liu, H., N. Lu, H. Jiang, J. Qin, and L. Yao. 2020. "Filling Gaps of Monthly Terra/MODIS Daytime Land Surface Temperature Using Discrete Cosine Transform Method." *Remote Sensing* 12: 361. https://doi.org/10.3390/rs12030361.

Lv, H., G. Wang, W. Xu, Y. Zhang, and L. Jiang. 2023. "Seasonal Variability of Satellite-Derived Primary Production in the South China Sea from an Absorption-Based Model." *Frontiers in Marine Science* 10: 1087604. https://doi.org/10.3389/fmars.2023.1087604.

Marchese, C., S. Colella, V. E. Brando, M. L. Zoffoli, and G Volpe. 2024. "Towards Accurate L4 Ocean Colour Products: Interpolating Remote Sensing Reflectance Via Dineof." *International Journal of Applied Earth Observation and Geoinformation* 135: 104270.

Martinez, E., A. Brini, T. Gorgues, L. Drumetz, J. Roussillon, P. Tandeo, G. Maze, and R. Fablet. 2020. "Neural Network Approaches to Reconstruct Phytoplankton Time-Series in the Global Ocean." *Remote Sensing* 12: 4156. https://doi.org/10.3390/rs12244156.

Mélin, F., G. Zibordi, and J.-F. Berthon. 2007. "Assessment of Satellite Ocean Color Products at a Coastal Site." *Remote Sensing of Environment* 110: 192–215. https://doi.org/10.1016/j.rse.2007.02.026.

Mikelsons, K., and M. Wang. 2019. "Optimal Satellite Orbit Configuration for Global Ocean Color Product Coverage." *Optics Express* 27: A445–A457. https://doi.org/10.1364/OE.27.00A445.

Minu, P., V. Souda, S. Baliarsingh, R. Dwivedi, Y. Ali, and P. Ashraf. 2020. "Assessing Temporal Variation of Coloured Dissolved Organic Matter in the Coastal Waters of South Eastern Arabian Sea." *Acta Oceanologica Sinica* 39: 102–109. https://doi.org/10.1007/s13131-020-1534-z.

Modi, A., M. Roxy, and S. Ghosh. 2022. "Gap-Filling of Ocean Color over the Tropical Indian Ocean Using Monte-Carlo Method." *Scientific Reports* 12: 18395. https://doi.org/10.1038/s41598-022-22087-2.

Mueller, J. L., C. Davis, R. Arnone, R. Frouin, K. Carder, Z. Lee, R. Steward, S. Hooker, C. D. Mobley, and S. McLean. 2000. Above-water Radiance and Remote Sensing Reflectance Measurements and Analysis Protocols. Ocean Optics Protocols for Satellite Ocean Color Sensor Validation, Revision 2 G. S. Fargion and J. L. Mueller, eds. 298–107, NASA Goddard Space Flight Center.

Neeley, A. R., and A. Mannino, IOCCG. 2018. Inherent Optical Property Measurements and Protocols: Absorption Coefficient. In *IOCCG Ocean Optics and Biogeochemistry Protocols for Satellite Ocean Colour Sensor Validation* 78. Dartmouth, NS, Canada: International Ocean-Colour Coordinating Group (IOCCG).

Oliver, M. A., and R. Webster. 1990. "Kriging: A Method of Interpolation for Geographical Information Systems." *International Journal of Geographical Information System* 4: 313–332. https://doi.org/10.1080/02693799008941549.

Reynolds, R. W., and T. M. Smith. 1994. "Improved Global Sea Surface Temperature Analyses Using Optimum Interpolation." *Journal of Climate* 7: 929–948. https://doi.org/10.1175/1520-0442(1994)007<0929:IGSSTA>2.0.CO;2.

Ruddick, K., G. Neukermans, Q. Vanhellemont, and D. Jolivet. 2014. "Challenges and Opportunities for Geostationary Ocean Colour Remote Sensing of Regional Seas: A Review of Recent Results." *Remote Sensing of Environment* 146: 63–76. https://doi.org/10.1016/j.rse.2013.07.039.

Sathyendranath, S., and T. Platt. 1998. "Ocean-color model incorporating transspectral processes." *Applied Optics* 37: 2216–2227.

Schwarz, J. N., P. Kowalczuk, S. Kaczmarek, G. F. Cota, B. G. Mitchell, M. Kahru, F. P. Chavez, A. Cunningham, D. McKee, and P. Gege. 2002. "Two Models for Absorption By Coloured Dissolved Organic Matter (CDOM)." *Oceanologia* 44: 209–241.

Shen, S., G. G. Leptoukh, J. G. Acker, Z. Yu, and S. J. Kempler. 2008. "Seasonal Variations of Chlorophyll a Concentration in the Northern South China Sea." *EEE Geoscience and Remote Sensing Letters* 5: 315–319.

Shi, W., and M. Wang. 2010. "Characterization of Global Ocean Turbidity from Moderate Resolution Imaging Spectroradiometer Ocean Color Observations." *Journal of Geophysical Research: Oceans* 115: C11022.

Siegel, D., S. Maritorena, N. Nelson, D. Hansell, and M. Lorenzi-Kayser. 2002. "Global Distribution and Dynamics of Colored Dissolved and Detrital Organic Materials." *Journal of Geophysical Research: Oceans* 107: 21-21–21-14. https://doi.org/10.1029/2001JC000965.

Sirjacobs, D., A. Alvera-Azcárate, A. Barth, G. Lacroix, Y. Park, B. Nechad, K. Ruddick, and J.-M. Beckers. 2011. "Cloud Filling of Ocean Colour and Sea Surface Temperature Remote Sensing Products over the Southern North Sea By the Data Interpolating Empirical Orthogonal Functions Methodology." *Journal of Sea Research* 65: 114–130. https://doi.org/10.1016/j.seares.2010.08.002.

Son, S., and M. Wang. 2015. "Diffuse Attenuation Coefficient of the Photosynthetically Available Radiation Kd (PAR) for Global Open Ocean and Coastal Waters." *Remote Sensing of Environment* 159: 250–258. https://doi.org/10.1016/j.rse.2014.12.011.

Song, Z., X. He, Y. Bai, X. Dong, D. Wang, T. Li, Q. Zhu, and F. Gong. 2023. "Atmospheric Correction of Absorbing Aerosols for Satellite Ocean Color Remote Sensing over Coastal Waters." *Remote Sensing of Environment* 290: 113552. https://doi.org/10.1016/j.rse.2023.113552.

Stock, A., A. Subramaniam, G. L. Van Dijken, L. M. Wedding, K. R. Arrigo, M. M. Mills, M. A. Cameron, and F. Micheli. 2020. "Comparison of Cloud-Filling Algorithms for Marine Satellite Data." *Remote Sensing* 12: 3313. https://doi.org/10.3390/rs12203313.

Valente, A., S. Sathyendranath, V. Brotas, S. Groom, M. Grant, T. Jackson, A. Chuprin, M. Taberner, R. Airs, and D. Antoine. 2022. "A Compilation of Global Bio-Optical in Situ Data for Ocean-Colour Satellite applications–version Three." *Earth System Science Data Discussions* 2022: 1–61.

van Oostende, M., M. Hieronymi, H. Krasemann, B. Baschek, and R. Röttgers. 2022. "Correction of Inter-Mission Inconsistencies in Merged Ocean Colour Satellite Data." *Frontiers in Remote Sensing* 3: 882418. https://doi.org/10.3389/frsen.2022.882418.

Wang, T. 2025. Dataset—In Situ Remote Sensing Reflectance and Chlorophyll-a Measurements Matched with MODIS-Aqua in the South Sea China (2010–2020).

Wang, M., and S. W. Bailey. 2001. "Correction of Sun Glint Contamination on the SeaWiFS Ocean and Atmosphere Products." *Applied Optics* 40: 4790–4798. https://doi.org/10.1364/AO.40.004790.

Wang, M., S. Son, and L. W. Harding, Jr. 2009. "Retrieval of Diffuse Attenuation Coefficient in the Chesapeake Bay and Turbid Ocean Regions for Satellite Ocean Color Applications." *Journal of Geophysical Research: Oceans* 114.

Wang, H., Y. Zhou, and X. Li. 2025. "GDCM: Generalized Data Completion Model for Satellite Observations." *Remote Sensing of Environment* 324: 114760. https://doi.org/10.1016/j.rse.2025.114760.

Wang, Y., Z. Gao, D Liu, and R. Sensing. 2019. "Multivariate DINEOF Reconstruction for Creating Long-Term Cloud-Free chlorophyll-a Data Records from SeaWiFS and MODIS: A Case Study in Bohai and Yellow Seas, China." *IEEE Journal of Selected Topics in Applied Earth Observations and Remote Sensing* 12(5): 1383–1395.

Wang, T., Y. Sun, H. Su, and W. Lu. 2023. "Declined Trends of Chlorophyll a in the South China Sea over 2005–2019 from Remote Sensing Reconstruction." *Acta Oceanologica Sinica* 42: 12–24. https://doi.org/10.1007/s13131-022-2097-y.

Wang, G., D. Garcia, Y. Liu, R. De Jeu, and A. J. Dolman. 2012. "A Three-Dimensional Gap Filling Method for Large Geophysical Datasets: Application to Global Satellite Soil Moisture Observations." *Environmental Modelling Software* 30: 139–142. https://doi.org/10.1016/j.envsoft.2011.10.015.

Wang, T., P. Yu, Z. Wu, W. Lu, X. Liu, Q. P. Li, and B. Huang. 2021. "Revisiting the Intraseasonal Variability of chlorophyll-a in the Adjacent Luzon Strait with a New Gap-Filled Remote Sensing Data Set." *IEEE Transactions on Geoscience Remote Sensing* 60: 1–11.

Wei, J., Z. Lee, S. Shang, and X. Yu. 2019. "Semianalytical Derivation of Phytoplankton, CDOM, and Detritus Absorption Coefficients from the Landsat 8/OLI Reflectance in Coastal Waters." *Journal of Geophysical Research: Oceans* 124: 3682–3699. https://doi.org/10.1029/2019JC015125.

Welschmeyer, N. A. 1994. "Fluorometric Analysis of Chlorophyll a in the Presence of Chlorophyll B and Pheopigments." *Limnology and Oceanography* 39: 1985–1992. https://doi.org/10.4319/lo.1994.39.8.1985.

Werdell, P. J., B. A. Franz, S. W. Bailey, G. C. Feldman, E. Boss, V. E. Brando, M. Dowell, T. Hirata, S. J. Lavender, and Z. Lee. 2013. "Generalized Ocean Color Inversion Model for Retrieving Marine Inherent Optical Properties." *Applied Optics* 52: 2019–2037. https://doi.org/10.1364/AO.52.002019.

Werdell, P. J., L. I. McKinna, E. Boss, S. G. Ackleson, S. E. Craig, W. W. Gregg, Z. Lee, S. Maritorena, C. S. Roesler, and C. S. Rousseaux. 2018. "An Overview of Approaches and Challenges for Retrieving Marine Inherent Optical Properties from Ocean Color Remote Sensing." *Progress in Oceanography* 160: 186–212. https://doi.org/10.1016/j.pocean.2018.01.001.

Wilson, A. M., and W. Jetz. 2016. "Remotely Sensed High-Resolution Global Cloud Dynamics for Predicting Ecosystem and Biodiversity Distributions." *PLoS Biology* 14: e1002415. https://doi.org/10.1371/journal.pbio.1002415.

Yang, C., H. Ye, and S. Tang. 2020. "Seasonal Variability of Diffuse Attenuation Coefficient in the Pearl River Estuary from Long-Term Remote Sensing Imagery." *Remote Sensing* 12: 2269.

Yu, X., Z. Lee, F. Shen, M. Wang, J. Wei, L. Jiang, and Z. Shang. 2019. "An Empirical Algorithm to Seamlessly Retrieve the Concentration of Suspended Particulate Matter from Water Color Across Ocean to Turbid River Mouths." *Remote Sensing of Environment* 235: 111491. https://doi.org/10.1016/j.rse.2019.111491.

Zibordi, G., K. Ruddick, I. Ansko, G. Moore, S. Kratzer, J. Icely, and A. Reinart. 2012. "In Situ Determination of the Remote Sensing Reflectance: An Inter-Comparison." *Ocean Science* 8: 567–586. https://doi.org/10.5194/os-8-567-2012